Journal of Advanced Ceramics
先进陶瓷
ISSN 2226-4108
CN 10-1154/TQ
清华大学出版社 Tsinghua University Press
SciOpen

J Adv Ceram 2026, **15**: 9221369

https://doi.org/10.26599/JAC.2026.9221369

Research Article

Gradient nano-columnar crystallite engineering enabled $BaTiO_3/Ba(Zr_{0.2}Ti_{0.8})O_3/BaTiO_3$ sandwich films with superior energy storage performance via a low thermal budget

Huali Liu[1,†], Xing Zhao[2,†], Hanfei Zhu[1,*], Li Li[1], Ying Liu[1], Haijian Wang[1], Zhongshuo Xia[1], Jianting Li[3,*], Hua Tan[4], Hui Liu[5,*], Chenxi Li[1], Zixu Yang[1], Gang Liu[2,*]

[1]*School of Chemistry and Chemical Engineering, Qilu University of Technology (Shandong Academy of Sciences), Jinan 250353, China*

[2]*School of Materials & Energy, Southwest University, Chongqing 400715, China*

[3]*School of Mechanical Engineering, Qilu University of Technology (Shandong Academy of Sciences), Jinan 250353, China*

[4]*State Key Laboratory of Material Processing and Die & Mould Technology, Huazhong University of Science and Technology, Wuhan 430074, China*

[5]*Beijing Advanced Innovation Center for Materials Genome Engineering, University of Science and Technology Beijing, Beijing 100083, China*

*Corresponding authors.

E-mail: H. Zhu, zhf@qlu.edu.cn;

J. Li, lijianting@qlu.edu.cn;

H. Liu, huiliu@ustb.edu.cn;

G. Liu, liugang13@swu.edu.cn

Received: July 8, 2026; Revised: August 27, 2026; Accepted: August 28, 2026

清華大學出版社 Tsinghua University Press | SciOpen

Abstract: Ferroelectric thin-film capacitors exhibit significant applications in pulsed power systems due to their high power density and ultrafast charge/discharge capability. However, the inherent trade-off between polarization and breakdown strength in ferroelectrics fundamentally imposes challenges for co-optimization of recoverable energy density (W_{rec}) and efficiency (η), while also compromising energy storage stability. To address these challenges, a gradient nano-columnar crystallite engineered $BaTiO_3/Ba(Zr_{0.2}Ti_{0.8})O_3/BaTiO_3$ sandwich film was constructed enabled via a low thermal budget process of 200 ℃. This approach facilitates an unique microstructure featured by gradient-distributed nano-columnar crystallites in the amorphous-dominated matrix via a spatially-separated manner throughout the sandwich film, thereby effectively modulating polarization behavior, mitigating dielectric nonlinearity, and consequently boost the energy storage performance remarkably. Experimental results demonstrate that this sandwiched structure is endowed with an enhanced maximum polarization (P_{max}) while a small remnant one (P_r), and a much-delayed polarization saturation, which are accountable for a W_{rec} ~ 100.6 J/cm³ with an ultrahigh η ~ 90.9% at 6.1 MV/cm. Furthermore, these sandwich films displayed broad operating temperature (RT~150℃) and frequency (100 Hz ~ 10 kHz) stability, and especially robust cycling-reliability (2×10^9 cycles). Through an innovatively engineered sandwich heterostructure design coupled with a low thermal budget, simultaneous achievements of low-temperature compatibility and superior energy storage characteristics lays a foundation for those integrated energy storage devices.

Keywords: Energy storage; Gradient nano-columnar crystallites; Barium titanate; Sandwich thin film; Low-thermal-budget

1 Introduction

Compared to batteries and electrochemical supercapacitors, ferroelectric dielectric capacitors have emerged as core components in ultrafast pulsed power systems due to their ultrahigh power density, demonstrating significant application prospects in smart grids, electromagnetic weapons, and renewable energy storage systems [1-3]. With the rapid development of IoT and 5G technologies in recent years, there has been an increasingly urgent demand for miniaturized, highly-reliable energy storage devices, consequently elevating higher performance requirements for thin-film ferroelectric capacitors. The energy storage density and efficiency of a ferroelectric capacitor can be calculated from its characteristic polarization−electric field (*P*-*E*) loop using the following equations [4-6]: the stored energy density $W_c = \int_0^{P_m} E \mathrm{d}P$, the recoverable/ recyclable energy density $W_{rec} = \int_{P_r}^{P_m} E \mathrm{d}P$, thus the energy storage efficiency $\eta = \frac{W_{rec}}{W_c}$, where P_m and P_r are the maximum polarization and remnant one of the ferroelectrics, respectively, and E is the applied electric field. Consequently, the high recoverable energy density W_{rec} and efficiency η demand a large P_m, a low P_r and a durable applied field E. However, the inherent trade-off between the electric polarization P and endurable electric field E_b (that is breakdown electric field) in homogeneous ferroelectric materials fundamentally constrains the upper limit of recoverable energy density while preventing synergistic co-optimization with energy efficiency [7-9]. This bottleneck prevents the ferroelectric capacitors from a broader range of applications, and it is imperative to develop ferroelectric materials with superior energy storage performance, i.e., higher energy density and efficiency.

Barium titanate ($BaTiO_3$, BTO), as one of the most representative eco-friendly lead-free perovskite ferroelectric materials, has become a preferred choice for the high-performance ferroelectric capacitors due to its large dielectric constant ε_r, low dielectric loss, small remnant polarization P_r, and some BTO-based film capacitors have gained intensive research attention in recent

years. For example, Cheng *et al.* [10] constructed polydomain structures (polytwin & heterophase polydomains) in epitaxial $Ba(Zr_{0.2}Ti_{0.8})O_3$ films deposited on various non-Si oxide substrates (such as $SrTiO_3$ and $LaAlO_3$) at 650 ℃, with which they achieved the largest energy density of ~166 J/cm^3 in 350 nm-thick film and the highest efficiency of ~96% in 1.8 μm-thickness. Later, Ren *et al.* [11] demonstrated that the bimodal polymorphic nanodomains engineering in $Ba(Zr_{0.2}Ti_{0.8})O_3$ epitaxial films grown on $SrTiO_3$ at 650 ℃ yielded an enhanced energy density W_{rec} of ~103 J/cm^3 coupled with a high efficiency η of ~87%. Chen *et al.* [12] prepared A/B-site co-doped $(Ba_{0.3}Sr_{0.7})(Zr_{0.18}Ti_{0.82})O_3$ films sputtered at 550 ℃ with a post-annealing of 600 ℃ on Si substrate using an artificial "dead-layer", which achieved a large W_{rec} of 89.4 J/cm^3 and η of 65%. However, achieving precise modulation over the engineered phase structures in these above reported films evidently presents considerable challenges, and also the complex multi-element compositional film systems are prone to induce substantial fluctuations in their electrical properties. A more critical issue is that the prohibitively processing temperature exceeding 600 ℃ employed in these above reports, frequently coupled with the necessity for expensive single-crystal oxide substrates, pose a huge integration barrier for the mainstream complementary-metal-oxide-semiconductor (CMOS) Si-based compatible electronics [13,14], and as doing so will introduce irremediable damages or performance degradation in those large scale-integrated electronic components on Si at an undesirably high processing temperature.

To allow practical applications of these ferroelectric film capacitors, it is crucial to integrate them on Si at a processing temperature as low as possible, while still maintain superior energy storage performance. Our previous investigations have demonstrated such a possibility for sputtered $BaTiO_3$ and $(Ba,Sr)(Zr,Ti)O_3$ films deposited on Si substrates at a reduced thermal budget to be compatible with the Si process (350~400 ℃) [15-18]. The use of a lattice-matching, conductive oxide $LaNiO_3$ has promoted the formation of a (001)-textured columnar nanograin structure in these low-temperature processed films. Such an engineered nanostructure endows them with commendable overall energy storage performance for the $BaTiO_3$ films (W_{rec} ~ 130-229 J/cm^3, η ~ 69%-76% @ 350 ℃) [15,16] and

$(Ba,Sr)(Zr,Ti)O_3$ films (W_{rec} ~ 134-148 J/cm^3, η ~ 87%-88% @ 400 ℃) [17,18], respectively. Recently, Liu *et al.* successfully pushed the deposition temperature of $BaTiO_3$ films down to 200 ℃ by engineering the thickness of $LaNiO_3$ buffer layer, an achievement desirable for the future development of microelectronics [19]. And, this low-temperature processed $BaTiO_3$ film gives an energy density W_{rec} of 94.7 J/cm^3 and an efficiency η of 78.2% @ 4 MV/cm. Nevertheless, the energy storage properties of ferroelectric films, including energy storage density and efficiency, typically tends to degrade when processed at a lower temperature. Such the degradation is primarily associated with their inferior electric polarization under low-temperature processing conditions. So, a critical and practical challenge remains in achieving further substantial enhancements in energy storage properties of ferroelectric films under thermal budgets as low as possible (preferably ≤ 300 ℃).

To address these challenges, building upon our prior studies on modulating the electrical properties of $BaTiO_3/BiFeO_3$ layered film heterostructures [20,21] and incorporating insights from the above reported works on low-temperature processing for ferroelectric film growth [15-18], this study successfully constructed the $BaTiO_3/Ba(Zr_{0.2}Ti_{0.8})O_3/BaTiO_3$ (BTO/BZT/BTO) sandwich films via radio-frequency magnetron sputtering technique with an ultra-low thermal budget of 200 ℃. An unique microstructure formed in this sandwich film at an ultra-low processing temperature, featured by gradient-distributed nano-columnar crystallites in an amorphous-dominated matrix via a spatially-separated manner, effectively tailored its polarization behavior, reduced the dielectric nonlinearity, and yielded an extremely slim *P-E* hysteresis loop. Concurrently, the electrical breakdown endurance can be greatly enhanced. As a result, this approach achieved a synergistic enhancement of high recoverable energy density (W_{rec} ~ 100.6 J/cm^3) and ultrahigh efficiency (η ~ 90.9%), along with an enhanced breakdown electric field E_b of 6.1 MV/cm. What's more, this low-thermal-budget sandwich film exhibited good energy storage stability, demonstrated by a broad operating frequency and temperature ranges (100 Hz ~ 10 kHz, 25~150 ℃), and especially, a fatigue endurance up to 2 × 10^9 cycles. Therefore, this BTO/BZT/BTO sandwich film processed with a low thermal budget shows a strong

application potential for high-power pulsed systems and high-energy-density integrated electronic devices.

2 Experimental

2.1 Deposition of BTO/BZT/BTO sandwich films

In this study, radio-frequency (RF) magnetron sputtering technique was used to prepare BTO/BZT/BTO sandwich films and the SiO_2-coated (100)Si single crystal served as the substrate of the films. The vacuum chamber was initially evacuated to a base pressure of 2×10^{-4} Pa, and the substrate was set to the desired temperature. Subsequently, the sputtering deposition of the Pt layer was carried out on the substrate as the bottom electrode. Notably, a thin Ti interlayer was deposited between the Pt electrode and the substrate so as to enhance their interfacial adhesion. Following the deposition of the Pt electrode layer, a $LaNiO_3$ (LNO) buffer layer was then sputtered onto the Pt layer, which can be used to reduce the deposition temperature and control the crystallographic orientation of the film. Finally, the BTO, BZT, and BTO layers were sequentially deposited on the LNO-buffered Pt/Ti/SiO_2/Si substrate, thus forming the BTO/BZT/BTO sandwich heterostructure. Table 1 summarizes the detailed processing parameters for each layer of the sandwich films. Note that the single BTO and BZT thin films were also prepared using the same processing conditions to facilitate the discussions of relevant issues in this study.

Table 1 Deposition parameters of BTO/BZT/BTO films via RF magnetron sputtering.

Parameters	Ti	Pt	LNO	BTO/BZT/BTO
Deposition temperature (°C)	300	300	300	200
Sputtering power (W)	55	55	100	100
Sputtering pressure (Pa)	0.3	0.3	0.3	1.2
Target-substrate distance (mm)	50			
Deposition time (min)	5	15	25	22.5/45/22.5
Post-deposition cooling rate (°C/min), atmosphere & pressure (Pa)	5, O_2 & 2.5			

2.2 Structural characterizations

The crystal structure and crystallographic orientation of BTO/BZT/BTO sandwich film was analyzed using X-ray diffractometer (XRD, Rigaku SmartLab SE 9kW with a Ni-filtered Cu Kα radiation). The surface and cross-sectional morphologies were characterized by field-emission scanning electron microscopy (SEM, ZEISS Sigma360, Germany) and the nanoscale microstructures of the film were investigated via transmission electron microscopy (TEM, Talos F200X G2, Thermo Scientific). The piezoelectric topography and domain switching behavior of the films were analyzed via piezoresponse force microscopy (PFM), using a MFP-3D Origin+ Atomic Force Microscope (AFM, Asylum Research, Oxford Instruments).

2.3 Electrical measurements

To perform the electrical characterizations, circular gold electrodes with a diameter of 200 μm were deposited on the film surface through a shadow mask. The bipolar/unipolar polarization-electric field (*P*-*E*) hysteresis loops, polarization currents, and leakage current curves of the films were measured using a Radiant Precision Multiferroic II ferroelectric tester. Moreover, the polarization responses under varying frequencies and charge-discharge cycling numbers were evaluated. The electric breakdown strength was analyzed through a two-parameter Weibull distribution model based on the measured *P*-*E* data. The frequency- and electric field-dependent dielectric properties were characterized using a high-precision impedance analyzer (TH2838H, Tonghui Electronics). The ferroelectric and dielectric behaviors as function of temperature were measured by integrating the ferroelectric tester and impedance analyzer with a temperature-controlled probe station (HFS600E-PB2, Linkam, UK), respectively.

2.4 Finite element simulations

Electric breakdown analyses of the BTO, BZT and BTO/BZT/BTO films were performed using COMSOL Multiphysics software. The propagation of electric tree channels in these films were simulated and analyzed using a stochastic breakdown model. The specific simulation details are provided in Supplementary Materials.

3 Results and discussion

3.1 Phase structure and fundamental electrical characteristics

The crystallization characteristics of BTO, BZT and BTO/BZT/BTO thin films deposited on LNO-buffered Pt/Ti/SiO_2/Si(100) substrate were analyzed by XRD 2θ-scan patterns. As clearly shown in Figure 1(a), the XRD patterns reveal that all films exhibit several diffraction peaks with no observable impurity phases. However, the attenuated peak intensities of these films relative to the Si substrate and Pt electrode signals may indicate diminished grain size along with a lower degree of crystallization at this low processing temperature of 200 ℃ (as will be directly observed by transmission electron microscopy below). What's more, the only (*l*00) diffraction peaks observed in these films reveal a preferred (100) crystallographic orientation, which is actually a consequence of induced preferential growth by the conductive LNO buffer layer. Such the LNO buffer-induced (100) preferred orientation has been demonstrated in our earlier studies on BTO and BFO thin film systems [15,19,20,22]. According to the reported literature [23,24], the conductive LNO thin film with a (100) crystallographic orientation can be crystallized on platinized Si(100) at a deposition temperature as low as 200 ℃. Meanwhile, as revealed by the XRD pattern and magnified view in Fig. 1(b), the diffraction peaks of the BTO film, the BTO/BZT/BTO sandwich film, and the BZT film exhibit a successive shift toward lower 2θ angles. This experimental observation may reflect the coexistence of Zr substitution-induced lattice expansion and interfacial compressive stress effects caused by the difference of Zr/Ti ion radius and the lattice mismatch of BTO/BZT layer, respectively. As previously reported in our works [15,22,25], a compressive internal stress can be induced within the film under a low processing temperature (200 ℃ in present case), which is dictated by a larger initial lattice misfit between the BZT film and the platinized Si substrate, compared to that of the BTO film under the same conditions. Such the combined contribution of Zr substitution-induced local lattice expansion/distortion and interfacial compressive stress effects would be expected to promote increased maximum polarization (P_{max}) of the BTO/BZT/BTO sandwich film, thereby enhancing the energy

storage characteristics.

The pole figure analyses can offer a further visualized evaluation of the film's preferred growth quality and grain orientation distribution. As depicted clearly in Fig. 1(c) and Note S1&Fig. S1 (Supplementary Materials), the pole figures are measured by using a fixed 2θ angle corresponding to the (200) diffraction peak for the BTO, BZT and BTO/BZT/BTO thin films. During the measurement, the samples are rotated by changing the tilt angle (χ, 0~75°) and the azimuthal angle (ϕ, 0~360°) with respect to the scattering vector. All the films exhibit similar pole figure mapping with a concentric ring located at the origin (χ, ϕ = 0°), revealing a (100) preferred orientation that consistent with the XRD data. As shown in Fig. 1(c) and supplementary Fig. S1, an additional observation of these pole figures is that, in comparison with the BTO film (χ, 0~8°), a narrower tilt angle spread of grains is observed in the BZT (χ, 0~3°) and BTO/BZT/BTO film (χ, 0~5°). This phenomenon is likely associated with the enhanced in-plane compressive stress in both films, facilitating a more concentrated grain orientation distribution.

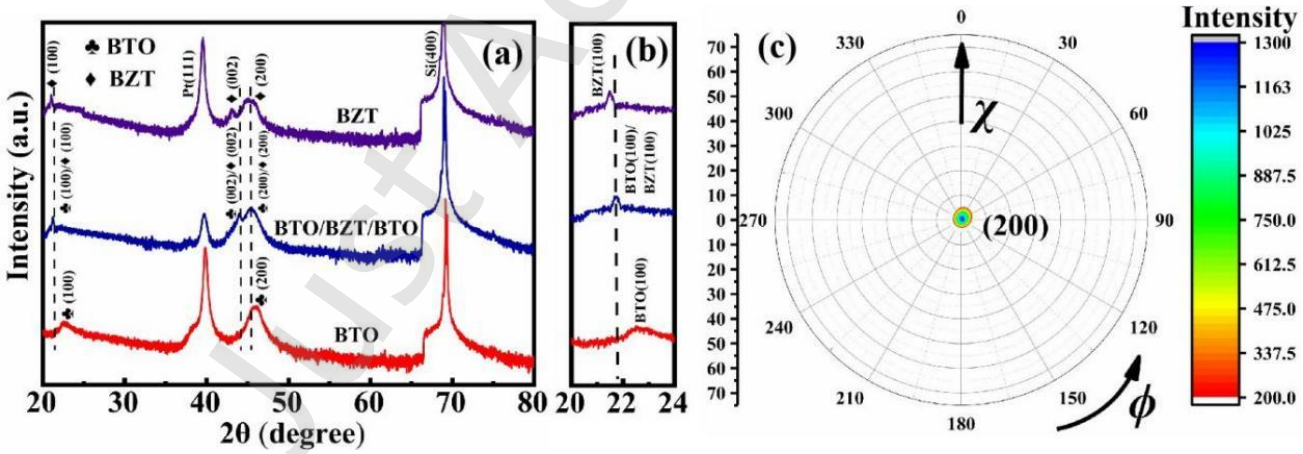

Fig. 1 (a) XRD patterns of the BTO, BZT and BTO/BZT/BTO thin films deposited on LNO-buffered Pt/Ti/SiO_2/Si substrates. (b) Magnified view of (100) diffraction peaks at around 2θ ~ 22° in (a). (c) Pole figure of the BTO/BZT/BTO sandwich film recorded at fixed 2θ for the (200) diffraction peak.

Following the preliminary crystallographic characterizations of the BTO, BZT, and BTO/BZT/BTO films by XRD above, we now focus on their various electrical properties to better understand the energy storage performance presented in the subsequent sections of this work. It should

be briefly noted in advance here that, as shown in Note S2 & Fig. S2 (Supplementary Materials), the single BTO and BZT films prepared in this study have approximately the same thickness as the BTO/BZT/BTO sandwich film (presented in Fig. 5(a) below), with the respective thicknesses being ~600 nm, ~627 nm, and ~632 nm, to facilitate the subsequent comparison and analysis of their electrical properties. Figure 2(a) presents the *P*-*E* hysteresis loops of BTO, BZT, and BTO/BZT/BTO films under the same applied electric field of 4 MV/cm. It should be pointed out here that, as illustrated in Note S3,S4 & Fig. S3(b),(d) (Supplementary Materials), this value of ~4 MV/cm represents the maximum endurable electric field (i.e., breakdown electric field E_b) for the BZT film in this study. Evidently, at the same applied electric field, the BZT film shows relatively pronounced ferroelectricity with a high maximum polarization (P_{max}), while both the BTO and BTO/BZT/BTO films demonstrate a predominantly linear polarization response, featuring reduced polarization but a significantly enhanced breakdown field strength E_b (as illustrated in supplementary Note S3 & Fig. S3(a),(c)). Another important aspect is presented in Fig. 2(b), which gives the dielectric constant versus measured electric field (ε_r-*E*) curves for the three films at the same electric field of 2 MV/cm with a scanning frequency of 1 MHz. The butterfly-shaped curve of BZT film signifies its dominant ferroelectric response, while the near-overlapping forward and backward sweeping ε_r-*E* curves of the BTO and BTO/BZT/BTO films indicate an attenuated ferroelectric response, i.e., an improved linear dielectric behavior. The dielectric tunability derived from ε_r-*E* curve, $\tau = \frac{\varepsilon_r(0) - \varepsilon_r(E)}{\varepsilon_r(0)} \times 100\%$ [17], shows that the BTO/BZT/BTO sandwich film exhibits a clearly reduced tunability of τ~14.2% compared to that of the BZT film (τ~18.3%), though it remains slightly higher than that of the BTO film (τ ~ 8.9%). As discussed in some previous reports [17,26,27], the smaller τ value validates the existence of a stronger linear dielectric response in the film corresponding to a linear-like *P*-*E* loop, which significantly contributes to the enhanced energy storage properties with high recoverable energy density W_{rec} and efficiency η, especially guarantees its energy storage stability against changes in various working conditions including temperature, frequency and charge/discharge cycle.

Fig. 2(c) depicts the leakage current density versus electric field (*J-E*) curves of the three films measured at the same electric field of 1.35 MV/cm, apparently in comparison with that of the BZT film (~10^{-5} A/cm^2), the BTO/BZT/BTO sandwich film achieves the reduced current density of 2.1×10^{-6} A/cm^2 approaching that of the BTO film (1.2×10^{-6} A/cm^2), which surely facilitates the improved breakdown field strength. With reference to prior pertinent works [28-30], the suppressed leakage current characteristics of the sandwich BTO/BZT/BTO heterostructure are likely correlating with the modified internal electric field distribution and interfacial potential barriers enabled by the improved in-plane compressive stress evidenced by the aforementioned XRD results. Additionally, as demonstrated in Note S5 & Fig. S4 (Supplementary Materials), a dominant bulk-controlled Ohmic leakage conduction behavior was revealed in these three films, whether in the positive (POS) or negative (NEG) electric field, implying a negligible impact of film-electrode contact effects on their electrical properties. The frequency-dependent dielectric constants (ε_r) and losses (tanδ) of these three films shown in Fig. 2(d) reveal that the BTO/BZT/BTO sandwich film has a dielectric constant ε_r that lies between that of BTO and BZT films, being close to that of BTO film but lower than that of BZT across the measured frequency range (20 Hz ~ 2 MHz). This observation supports that the sandwich film configuration exhibits the behavior analogous to a series-connected capacitor model ($\frac{1}{C_{\text{total}}}=\sum_i\frac{1}{C_i}$), where the voltage-division law of $V_i=(\frac{C_{\text{total}}}{C_i})V_{\text{total}}$ enables the BTO/BZT/BTO sandwich film to withstand a higher applied voltage while delaying the saturation of electric polarization, thereby deliver an enhanced breakdown electric field E_b. Concurrently, and consistent with the leakage current results, the BTO/BZT/BTO film also shows the small losses (tanδ < 0.03) across the whole frequency range, further corroborating its improved resistance to electric breakdown. Collectively, these combined dielectric behavior and leakage current characteristic further imply that the BTO/BZT/BTO sandwich film can be expected to possess the enhanced energy storage performance, which will be presented in the section below.

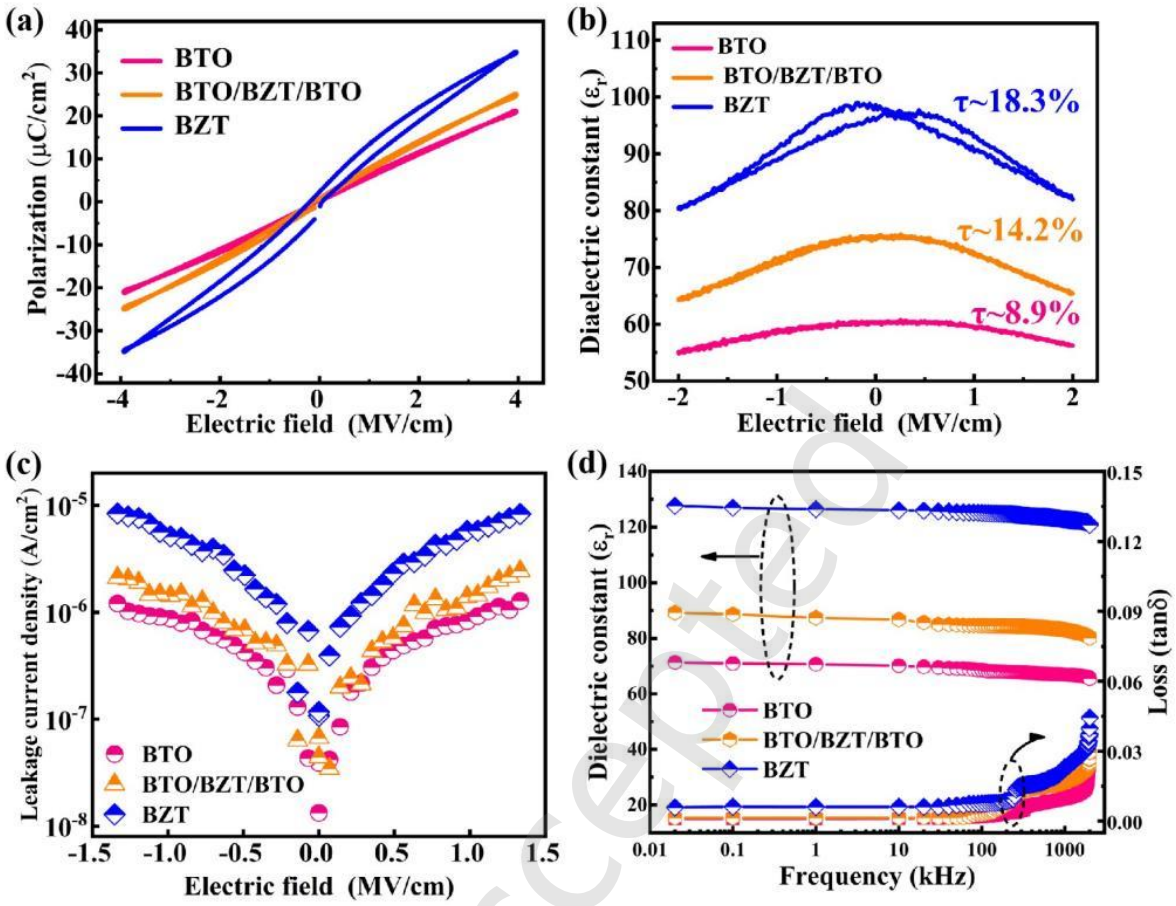

Fig. 2 Comprehensive electrical properties of BTO, BZT and BTO/BZT/BTO films: (a) polarization-electric field (*P*-*E*) hysteresis loops under the same applied electric field of 4 MV/cm; (b) electric field dependent dielectric constant (ε_r-*E*) curves; (c) leakage current densities; and (d) dielectric constant ε_r & loss tangent tanδ as function of measuring frequency.

3.2 Polarization relaxation response and energy storage performance

The polarization relaxation response of ferroelectric materials, i.e., the temporal evolution of polarized domain after removal of an applied bias voltage, undoubtedly has an impact on their energy storage characteristics. This behavior is evaluated for the BTO, BZT and BTO/BZT/BTO films using piezoresponse force microscopy (PFM). As shown in Figure 3, a preset bias voltage of ±30 V is applied via PFM tip to a specific area on the film surface to "write" the domain pattern, followed by "reading" the domain topography in the corresponding area after a relaxation duration of 15 minutes in present case. Evidently, these three films initially exhibit a specific preset domain topography. Specifically, as

can be seen from the PFM amplitude images given in Fig. 3(a)-(c), a distinguishable domain switching pattern is observed in the BTO/BZT/BTO sandwich film, despite its pattern intensity being somewhat weakened relative to that of the BZT film. By contrast, the BTO film shows no observable domain switching pattern, implying its significantly lower polarization. After the same relaxation duration of 15 minutes, as clearly demonstrated in Fig. 3(d)-(f), the BZT film still retains a detectable yet weak domain switching pattern, whereas the pattern of the BTO/BZT/BTO sandwich film almost disappear, leaving no observable domain topography remnants. Correspondingly, as shown in Fig. 3(g)–(i), the PFM butterfly (amplitude–voltage) curves of the three films are presented under the initial state and after a relaxation duration of 15 min. These curves exhibit a trend consistent with the topographical features of the corresponding films described above. The butterfly amplitude decreases from the BZT film to the BTO/BZT/BTO sandwich film, and is extremely small for the BTO film. Specifically, the BZT film in the initial state displays a thin and narrow butterfly curve, which is markedly different from the typical butterfly curves observed in conventional ferroelectrics. Even after a relaxation duration of 15 min, a certain residual butterfly-shaped amplitude signal remains observable. While the BTO/BZT/BTO sandwich film, after experiencing the same duration process as the BZT film, almost no obvious butterfly amplitude signal can be detected. As for the BTO film, regardless of whether in the initial state or after the relaxation duration process, no distinct butterfly curve is exhibited, instead, the amplitude–voltage curve remains nearly flat with negligible voltage dependence, indicating a weakly crystallized or amorphous-dominated structural characteristic. Collectively, the temporal evolution of domain topography after "writing" indicate a more rapid polarization relaxation in the BTO/BZT/BTO film before and after poling under the same applied bias voltage. This faster domain switching and recovery capability contributes to a "linear-like" slim *P-E* loop with an enhanced effective polarization (ΔP, i.e. $P_{max} - P_r$), thereby significantly improving the energy storage density and efficiency. These results are well agree with the discussions of their *P-E* loops presented above. Note that, as shown in Fig. S5 (Supplementary Materials), the above discussions also holds true for

the PFM phase images of these three films, confirming the consistency of our observations.

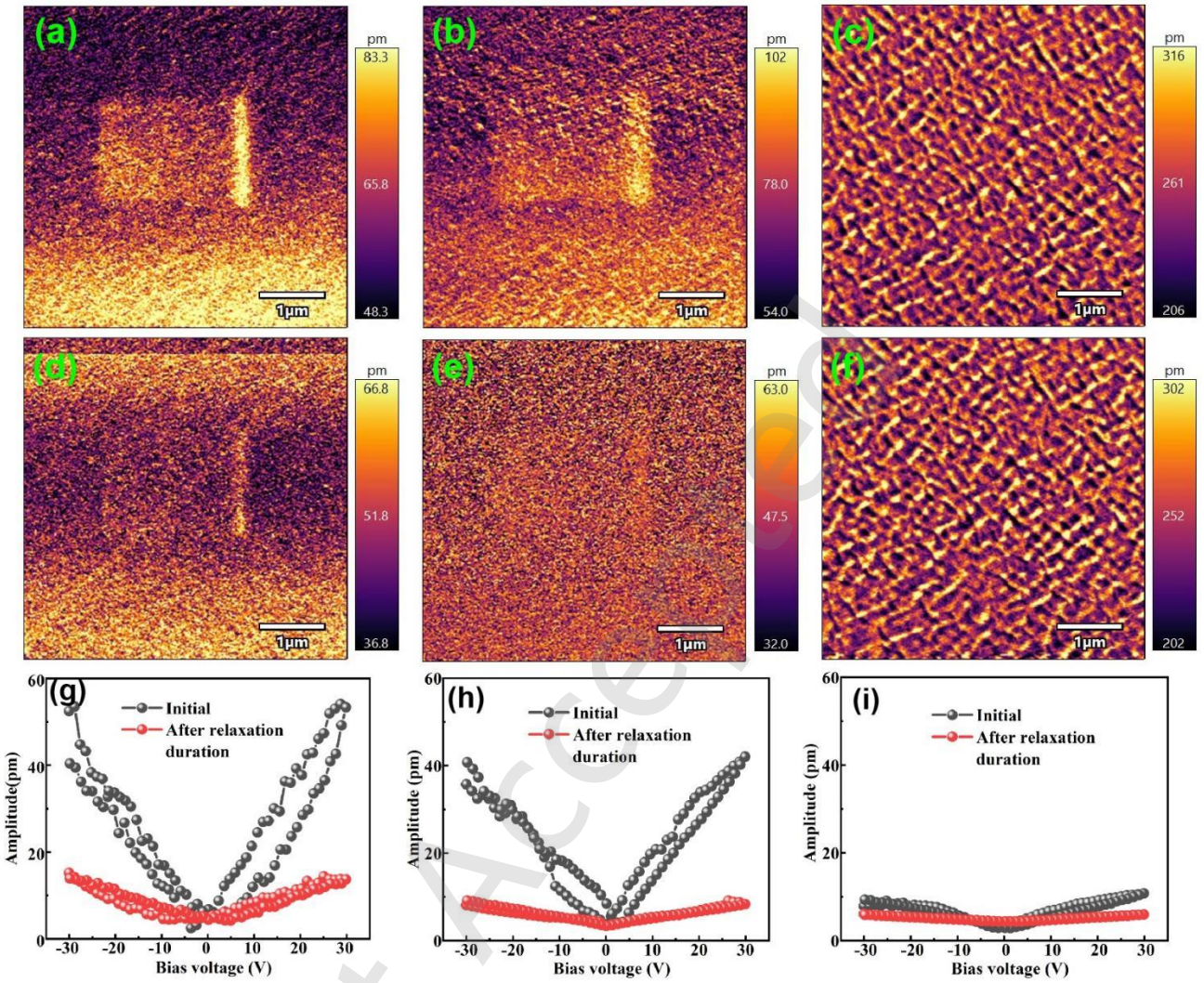

Fig. 3 PFM amplitude images of domain configuration initial (top panel) and after a relaxation duration of 15 min (middle panel) for (a) & (d) BZT, (b) & (e) BTO/BZT/BTO, (c) & (f) BTO films. (g) – (i) show the corresponding PFM butterfly curves (bottom panel) of films under the initial and after a relaxation duration of 15 min.

Building on the systematic discussions above on the crystal structures and comprehensive electrical properties of the BTO, BZT and BTO/BZT/BTO thin films, we now turn our attention to their energy storage performance as evaluated by *P-E* loop measurements at the maximum applied electric field E_{max}, i.e., approximately the breakdown electric field E_b. According to the *P-E* loops of the single BTO and BZT thin films under their respective E_{max} shown in supplementary Note S3 and

Fig. S3(a) & (b), the BTO film gives an enhanced endurable applied electric field, although its polarization is reduced compared with that of the BZT film. By integrating these two components, that is, introducing a BZT film as an intermediate interlayer into the BTO matrix to form a sandwich film in this study, as shown in Figure 4(a), the BTO/BZT/BTO sandwich film exhibits a maximum polarization P_{max} of 38.0 μC/cm^2 and an enhanced E_{max} of 6.1 MV/cm. The notably weak polarization current peaks indicates its diminished ferroelectric characteristic. It can thus be concluded that the sandwich BTO/BZT/BTO film achieves a collective enhancement of effective polarization (P_{max}–P_r) and endurable electric field (E_{max}). This enhancement originates from the modification of polarization behavior enabled by the unique microstructure in the sandwich BTO/BZT/BTO heterostructure processed at an ultra-low temperature of 200 ℃. As will be deeply discussed in the subsequent TEM characterizations, this unique microstructure will contribute to superior energy storage properties of the sandwich film. As a result, the unipolar *P*-*E* loop in Fig. 4(b) demonstrates that the BTO/BZT/BTO sandwich film achieves an outstanding recoverable energy density (W_{rec}) of 100.6 J/cm^3 (marked by yellow shaded area), along with remarkably high efficiency (η) of 90.9%, which is clearly superior to those of the single BTO and BZT thin films presented in Fig. S3(c)&(d) (Supplementary Materials). The inset Weibull model in Fig. 4(b) validates its enhanced breakdown electric field E_b of 6.1 MV/cm, and a detailed description of the Weibull statistical model of electric breakdown behavior is provided in Note S4 (Supplementary Materials).

The temperature-dependent dielectric properties can offer further insights into the polarization behavior, complementing the *P*-*E* loop analysis. Fig. 4(c) presents the dielectric constant (ε_r) and loss (tanδ) of BTO/BZT/BTO thin film over a temperature range of 20–310 ℃. Under various measurement frequencies of 1 kHz, 10 kHz, 100 kHz and 1 MHz in present case, the dielectric constant shows a maximum with a broad peak at a certain temperature, accompanied by a slight shift of the peak with frequency (200 ℃ to 216 ℃, as indicated by the dashed arrow). This observed broad peak is likely associated with the dispersed nano-sized columnar crystallites embedded in the amorphous matrix of

the sandwich film (illustrated in detail in the TEM analyses below), which contributes to an insignificant frequency dispersion phenomenon in the BTO/BZT/BTO sandwich film. Additionally, Fig. 4(d) presents the fitted results of temperature-dependent dielectric constant (ε_r–T) curves of BTO/BZT/BTO thin film measured at various frequencies, enabling an analysis of its polarization response based on the modified Curie-Weiss relationship [31,32]:

$$\frac{1}{\varepsilon_r}-\frac{1}{\varepsilon_m}=\frac{(T-T_m)^{\gamma}}{C} \tag{1}$$

where ε_m is the maximum dielectric constant, T_m is the characteristic temperature corresponding to ε_m, and C is the Curie constant. The relaxation factors (γ) of the BTO/BZT/BTO sandwich film were thus obtained as 1.30~1.50 at various testing frequencies, which is obviously lower than that of typical relaxor ferroelectrics (γ~2). Combining the observed slight frequency dispersion effect in Fig. 4(c), the BTO/BZT/BTO sandwich film in this study tends to exhibit a predominantly near-linear polarization response with weakly relaxor-like component, indicating a suppression of the typical relaxor characteristics [32,33]. Consequently, a slim *P*-*E* loop featured by a substantially reduced remanent polarization (P_r) is observed, which facilitates fast domain switching and recovery, and consequently yields enhanced energy storage properties. These findings are in good agreement with the PFM analysis presented above. Additionally note that, the temperature-dependent dielectric properties of the BTO and BZT films, as well as the corresponding detailed discussions, have been provided in Fig. S6 and Note S6 (Supplementary Materials).

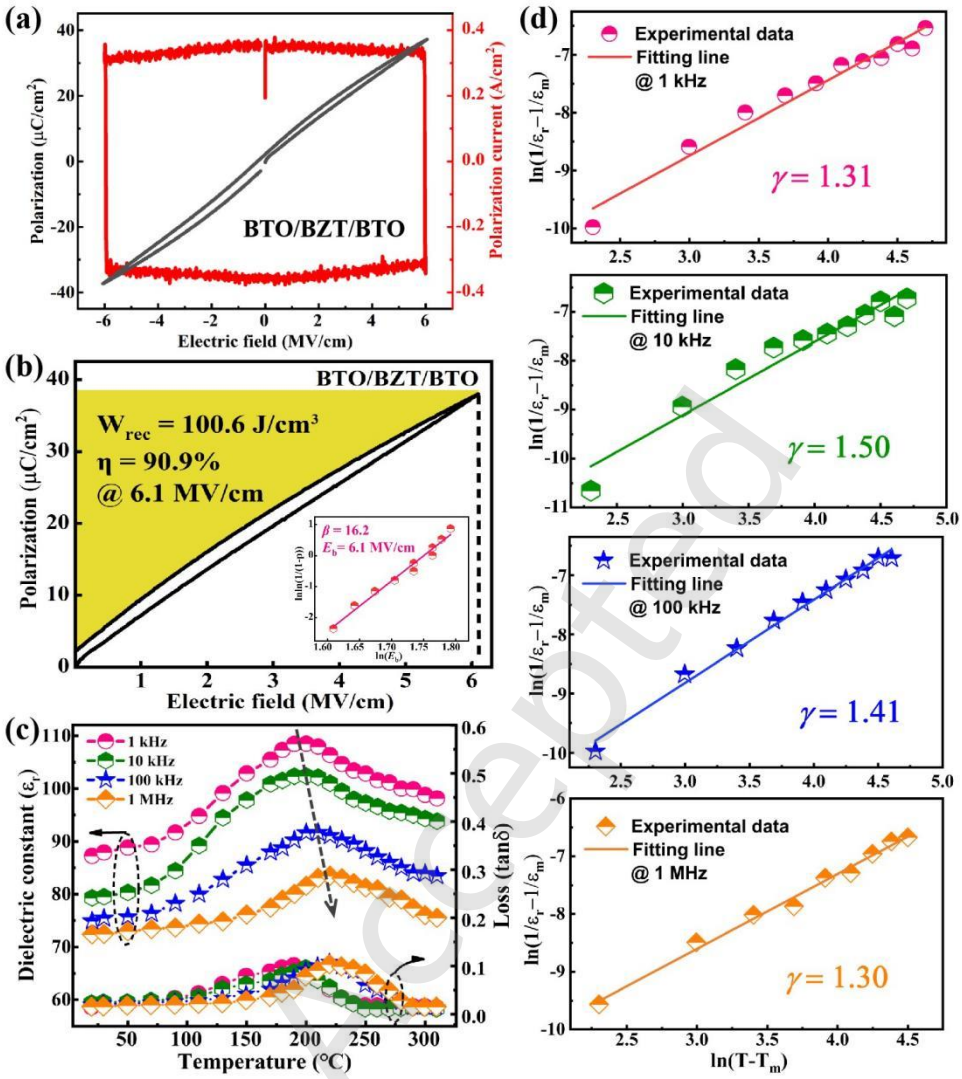

Fig. 4 (a) *P*-*E* loop and polarization current curve measured at an electric field of 6 MV/cm; (b) energy storage characteristics and inset shows the Weibull distribution plot demonstrating breakdown electric field E_b; (c) temperature-dependent dielectric constant ε_r & loss tangent tanδ; (d) corresponding fitting lines of ε_r-*T* curves shown in (c) of the BTO/BZT/BTO sandwich film.

3.3 Microstructure and dielectric breakdown behavior

Synthesizing the systematic discussions of electrical properties of the three thin films presented above, and to gain a deeper understanding of superior energy storage performance of the BTO/BZT/BTO sandwich film in this work, we now perform a nanoscale microstructural characterization and analysis in detail using transmission electron microscopy (TEM). As shown in Figure 5(a), the cross-sectional TEM image of BTO/BZT/BTO sandwich film heterostructure reveals

a sharp and clean interface between each layer from the top BTO layer to bottom SiO_2-coated Si substrate. Accordingly, the cross-sectional line-scan profiles of various elements and their corresponding EDS mapping clearly demonstrated in Fig. S7 (Supplementary Materials) correlate well with the layered-structure of the BTO/BZT/BTO film with a highly uniform elemental distribution throughout the whole film system, confirming without any elemental inter-diffusion between each layer. A closer examination from Fig. 5(a) reveals a more critical observation of structural feature, that is, there are some elongated, dark-contrast columnar regions distributed diffusely throughout the sandwich BTO/BZT/BTO film (as denoted by red arrows). These columnar regions are clearly well-defined and regularly arranged in the bottom BTO layer, and their prevalence decreases in the middle BZT layer. While in the top BTO layer, the contrast of columnar region diminishes substantially, with most areas displaying bright contrast instead. This systematic variation demonstrates a progressively descending gradient in both the abundance and contrast intensity of these columnar regions from the bottom BTO layer, through the intermediate BZT layer, to the top BTO layer. The high-resolution TEM (HRTEM) images obtained from different positions inside the BTO/BZT/BTO sandwich film shown in Fig. 5(b)-(f) provide an evidence that these dark-contrast elongated columnar regions are crystallized with an estimated average lateral width of 5~10 nm, thereby termed as nano-columnar crystallites in this study. Conversely, the regions exhibiting bright contrast in Fig. 5(a) are characterized by an amorphous or poorly-crystalline state. Specifically, as illustrated in Fig. 5(b) and (c), the HRTEM images taken from the two areas marked by the rectangular boxes I & II in Fig. 5(a) provide a detailed view of the bottom- and top-BTO/BZT interfaces (as marked by blue arrows). It is evident that the nano-columnar crystallites, identifiable by variably-shaped outlines using green dashed lines, are distributed at both interfaces. Some of these columnar crystallites extend across the interface into the adjacent layer, while others are terminated or blocked at the interface, and the large proportion of areas outside the dashed outlines are predominantly in an amorphous state. Moreover, the HRTEM images shown in Fig. 5(d)-(f) taken from the areas indicated by the boxes III, IV & V of Fig. 5(a) reveal that

the film bulk of top/bottom BTO cap layers and BZT intermediate layer share a consistent microstructural characteristic, wherein some elongated nano-columnar crystallites embedded in an amorphous-dominated matrix. Fig. 5(g), (h), (i) present the selected area electron diffraction (SAED) patterns corresponding to the HRTEM images of Fig. 5(d), (e), (f), respectively. It is evident that each layer of the film system exhibits diffuse and blurred diffraction ring accompanied by a few scattered diffraction spots. This observation further confirms the presence of nano-sized crystallization regions distributed spatial-separately in the predominant amorphous matrix. It is hereby noted that Note S7&Fig. S8 (Supplementary Materials) can intuitively support such the microstructural feature of the sandwich film at a more microscopic scale. Based on the above detailed microstructure analyses of BTO/BZT/BTO sandwich film, the volume fraction of nano-columnar crystallization regions in each layer can be semi-quantitatively estimated by distinguishing the contrast in brightness & darkness observed in the cross-sectional TEM image of Fig. 5(a). The used calculation method is elucidated in Note S8 (Supplementary Materials). As depicted in the inset of Fig. 5(a), the volume fractions of the nano-columnar crystallization regions in the bottom BTO, middle BZT and top BTO layers have been semi-quantitatively estimated to be ~54.5%, ~36.1% and ~22.9%, respectively. As a result, the BTO/BZT/BTO sandwich film experienced an ultra-low thermal budget of 200 ℃ in this study possesses an unique microstructure featured by a descending gradient of nano-columnar crystallites distributed in the amorphous-dominated matrix via a spatially-separated manner throughout the sandwich film system. Such the unique microstrcture of the BTO/BZT/BTO sandwich film is conducive to modifying its polarization response by mitigating the dielectric nonlinearity associated with ferroelectric behavior, as illustrated in Fig. 4 above, thereby giving rise to a slim *P*-*E* loop. This contributes to a delayed saturation of electric polarization, yielding a reduced remanent polarization (smaller P_r) while achieving a significantly improved breakdown electric field (higher E_b). Additionally, as discussed in the aforementioned XRD results, the in-plane compressive stress existing in the BTO/BZT/BTO sandwich heterostructure enables it to retain a reasonably high maximum

polarization P_{max}. Consequently, the synergy of these factors endows the BTO/BZT/BTO sandwich film with superior energy storage characteristics, that is concurrently enhanced energy storage density W_{rec} and efficiency η. It is worth further noting that the detailed investigation into energy storage stability of the BTO/BZT/BTO thin film will be provided later.

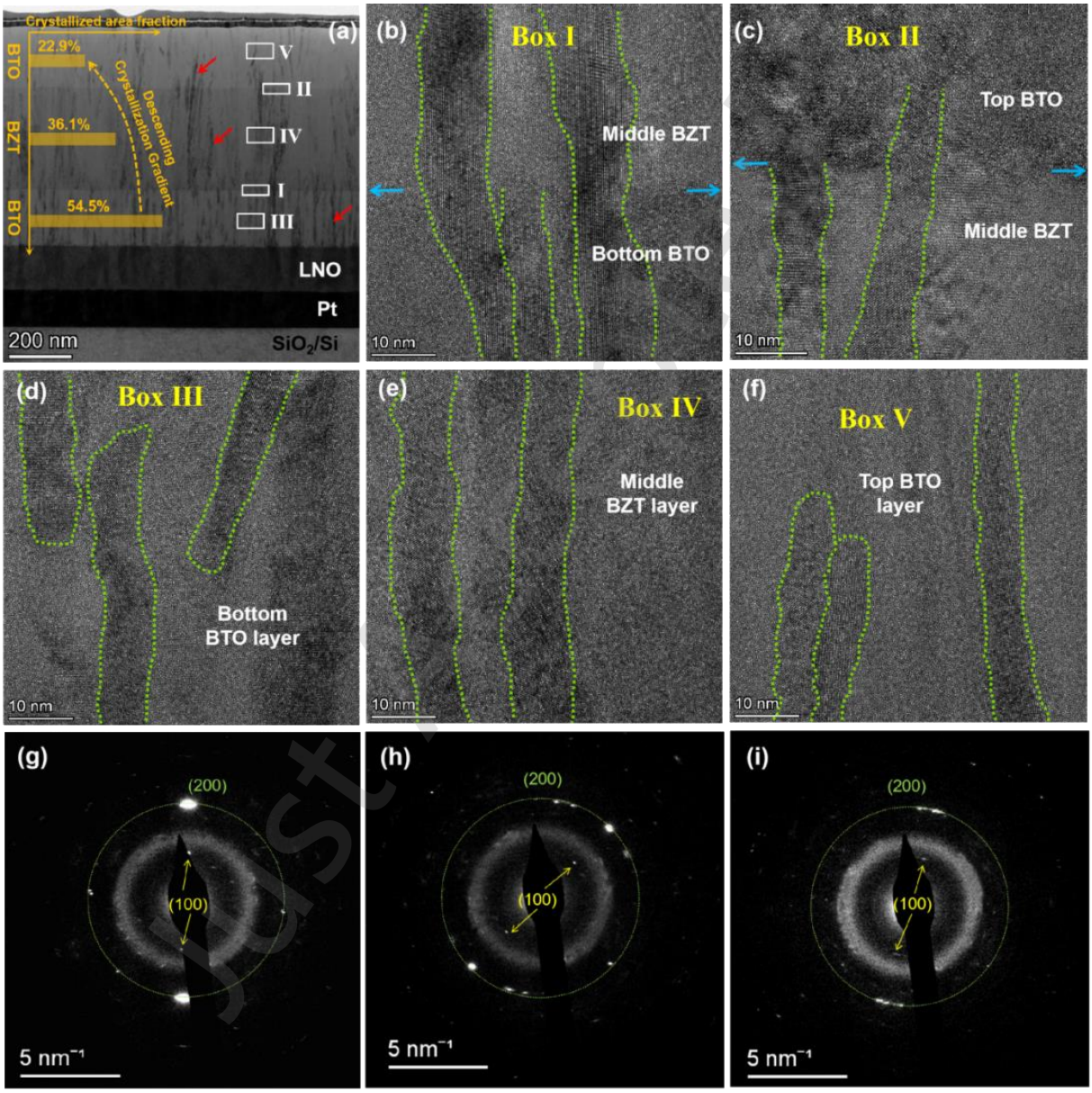

Fig. 5 (a) Cross-sectional TEM image of the BTO/BZT/BTO sandwich film. (b)-(f) HRTEM images corresponding to the box regions marked in (a), respectively. (g), (h), (i) Selected area electron diffraction (SAED) patterns obtained from (d), (e), (f), respectively.

Since such the unique microstructure featuring gradient nano-columnar crystallites distributed

separately within an amorphous phase-dominated matrix has been verified by the above TEM observations, the impact of this microstructural feature on the electric breakdown strength of dielectric energy storage films warrants further in-depth investigation. Therefore, numerical simulations based on finite element method (details are given in Note S9 in Supplementary Materials) were performed to discuss the role of the aforementioned microstructure in determining the propagation path of electrical trees and the local electric potential distribution in BTO/BZT/BTO sandwich film. Figure 6 gives the finite element simulation results of the sandwich film, where the elongated rectangles within each layer represent the nano-columnar crystallites possessing a relatively high dielectric constant, and the surrounding regions outside the elongated rectangles correspond to the amorphous matrix with a lower dielectric constant compared to these crystalline columnar grains. The number of elongated rectangles in each layer denotes the volume fraction of the columnar crystalline phase. Apparently, the crystalline phase ratio in the amorphous matrix exhibits a gradient decrease from the bottom BTO layer to the top BTO layer, thereby closely matching the observed TEM microstructure. The propagation path of electrical trees and corresponding local electric potential distributions in the BTO/BZT/BTO sandwich film at different time duration under an applied electric field were simulated. It can be observed from Fig. 6 that, as increasing the time duration, the electrical trees initiate from the top BTO layer and gradually propagate toward the bottom BTO layer. Because the numerous nano-sized columnar crystallites can store charges, the developing tree channels primarily tend to pass through or extend along the columnar crystallites and their adjacent regions. Correspondingly, a relatively high local electric potential is observed inside the columnar grains and at the interfaces between the columnar crystallites and the amorphous matrix, and such local potential becomes more pronounced with increasing columnar grain ratio. In contrast, the amorphous matrix exhibits a low potential distribution without any sign of charge concentration, indicating its high electric breakdown characteristics. In fact, this enhanced breakdown effect of the BTO/BZT/BTO film is closely associated with the interfacial barrier blocking effect between the amorphous matrix and the discretely

distributed columnar crystallites within each layer, as well as the obstruction at the electrically discontinuous BTO/BZT interfaces (which exhibit different dielectric constants). Similar phenomena have also been observed in some other thin-film heterostructures [34-36]. Considering the synergistic balance between the enhanced electric breakdown characteristics of the amorphous matrix and the polarization response of the dispersed nano-columnar crystallites, such an unique microstructure is favorable for achieving enhanced energy storage performance.

Additionally, the electric breakdown simulations were also performed for the single BTO and BZT films. Fig. S9 and S10 (Supplementary Materials) show the electrical tree propagation of the BTO and BZT films under an applied electric field, respectively. Evidently, compared with the BTO/BZT/BTO sandwich film, both films display an obvious short time duration of the electrical tree paths even under a slightly lower applied electric field, indicating an increased probability of electric breakdown. Collectively, the simulation results demonstrate that the gradient nano-columnar crystallites and the electrically discontinuous hetero-interfaces between adjacent layers in the BTO/BZT/BTO sandwich film act as barriers to the propagation of electrical trees, thereby leading to its enhanced breakdown strength.

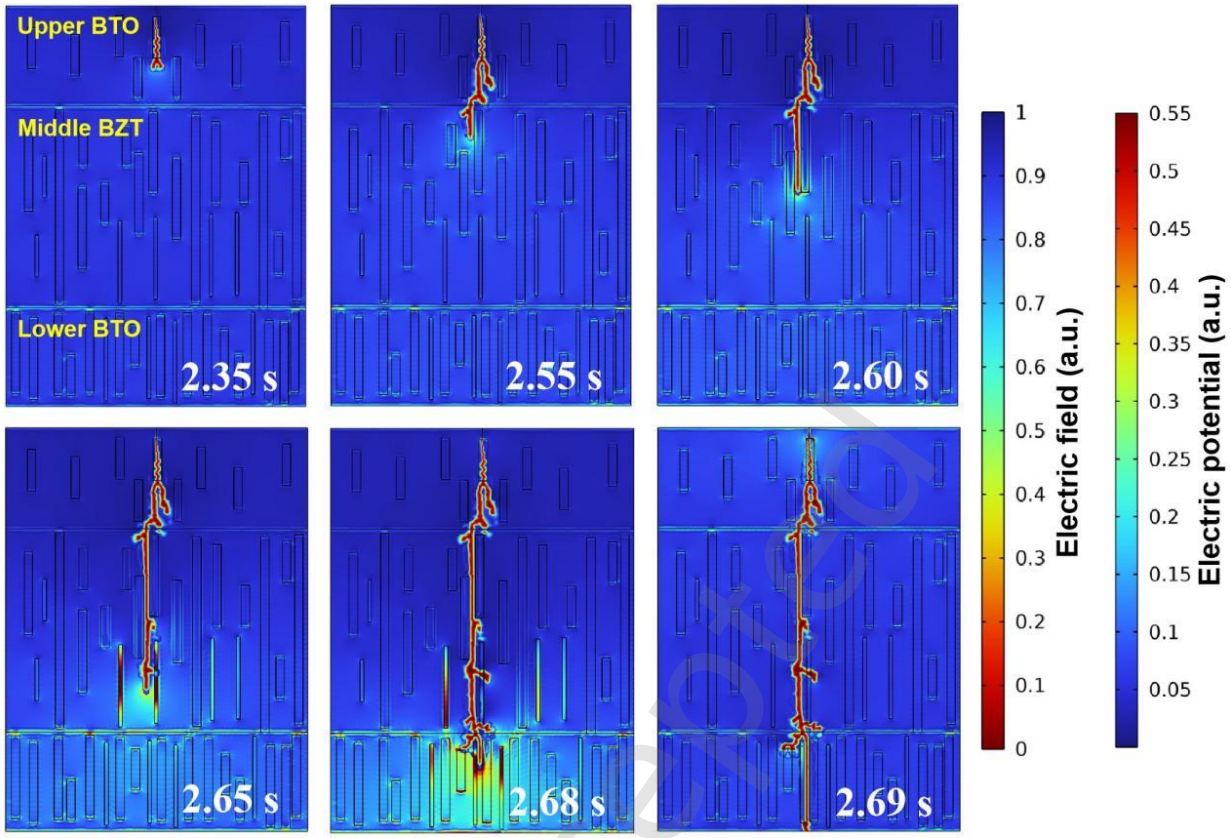

Fig. 6 Finite element simulations of electrical breakdown path propagation and electric potential distribution for the BTO/BZT/BTO sandwich film.

3.4 Comprehensive stability of energy storage performance

The energy storage stability of ferroelectric capacitors is undeniably crucial for their practical applications. Typically, the energy storage performance of ferroelectric materials is primarily governed by three key factors: operating temperature and frequency, as well as charging/discharging cycles. Figure 7 systematically presents the variations in recovery energy density (W_{rec}) and efficiency (η) of the BTO/BZT/BTO sandwich film in terms of frequency response, temperature adaptability, and cycling durability. Fig. 7(a) gives the room temperature (RT) *P-E* loops of BTO/BZT/BTO sandwich film measured at various frequencies under a fixed applied electric field of ~2 MV/cm, these *P-E* loops maintain nearly identical shapes across a broad frequency range (100 Hz to 10 kHz), with no discernible distortion such as loop tilting or widening. As illustrated in the corresponding Fig. 7(b), the minimal frequency dependence throughout the testing frequency range, evidenced by variations in W_{rec}

and η below 6% and 5%, respectively, confirms its good frequency stability. The temperature evolution of *P-E* loops and energy storage characteristics of the film measured at ~2 MV/cm are shown in Fig. 7(c) and (d), respectively. Throughout the operational temperature from 25 ℃ (RT) to 150 ℃, the polarization behavior basically maintains a consistency, showing negligible thermally induced disorder in *P-E* loops. Despite a somewhat degradation in both energy density ($\Delta W_{rec} < 7\%$) and efficiency ($\Delta\eta < 8\%$) with increasing temperature, the film maintains an impressive efficiency exceeding 90% even at 150 ℃, showing its good thermal adaptability for practical applications, such as hybrid electric vehicles (~140 ℃) and pitch control devices in wind-power-generation systems (~125 ℃) [37,38]. Furthermore, excellent cycling durability is essential for dielectric capacitors during long-term charging/ discharging cycling. Therefore, the cycling *P-E* loops of the film were performed at $E = 2$ MV/cm using a sine wave with a frequency of 500 kHz. Fig. 7(e) reveals that the BTO/BZT/BTO sandwich film preserves remarkable slim *P-E* loops even following 2×10^9 cycles, with negligible polarization degradation. Correspondingly, as given in Fig. 7(f), the ultra-low variations in energy density ($\Delta W_{rec} < 3\%$) and efficiency ($\Delta\eta < 1\%$) signify robust cycling endurance against long-term charging/discharging process. The convergence of these energy storage stability metrics across multiple operating conditions designates the sandwich BTO/BZT/BTO heterostructure as a great potential candidate for reliable, high-power-density energy storage devices. As the foregoing detailed discussions, the superior energy storage properties and stability against various operating conditions are closely relating with the modified polarization behavior of BTO/BZT/BTO sandwich film enabled by its unique microstructure of gradient nano-columnar crystallites engineering via an ultra-low thermal budget.

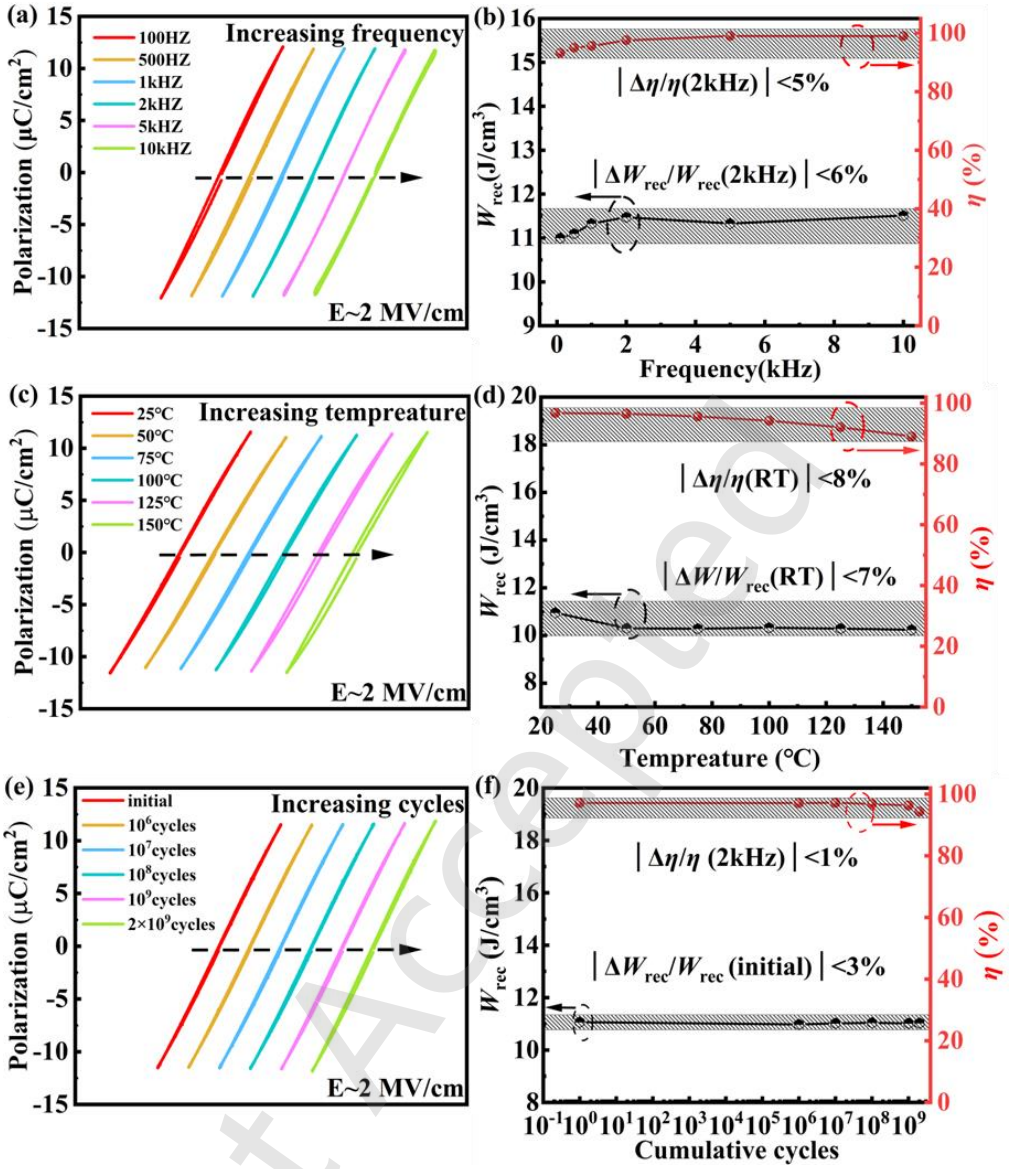

Fig. 7 The left panel shows the *P*-*E* loops of the BTO/BZT/BTO film as a function of (a) frequency, (c) temperature, and (e) charging/discharging cycles, respectively. The right panel gives the corresponding plots of (b) frequency, (d) temperature, (f) cycling dependent recoverable energy density (W_{rec}) and efficiency (η), which are calculated from their *P*-*E* loops. Note that, the W_{rec}(2kHz), W_{rec}(RT) and W_{rec}(initial) in (b), (d), (f) represent the W_{rec} measured at 2 kHz, at room temperature, before charge/discharge cycling, respectively, and the corresponding η are η(2kHz), η(RT) and η(initial).

Finally, Figure 8 systematically benchmarks the energy storage performance of the BTO/BZT/BTO sandwich film in this work against those reported representative BTO- and BZT-based thin films grown on Si substrates, encompassing doping, multilayer and solid solution systems

[12,27,39-51], with a primary focus on efficiency (η), cycling reliability, and processing temperature compatibility. This comparative analysis reveals that our sandwich BTO/BZT/BTO sandwich film demonstrates superior overall energy storage properties, exhibiting not only commendable W_{rec} ~ 101 J/cm^3, but more remarkably, outstanding efficiency (~91%), robust cycling endurance (2 × 10^9 cycles), and significantly reduced thermal budget requirements for integration compatibility (≤300 ℃ in our work). These remarkable attributes underscore its tremendous promise for applications of integrated energy storage devices.

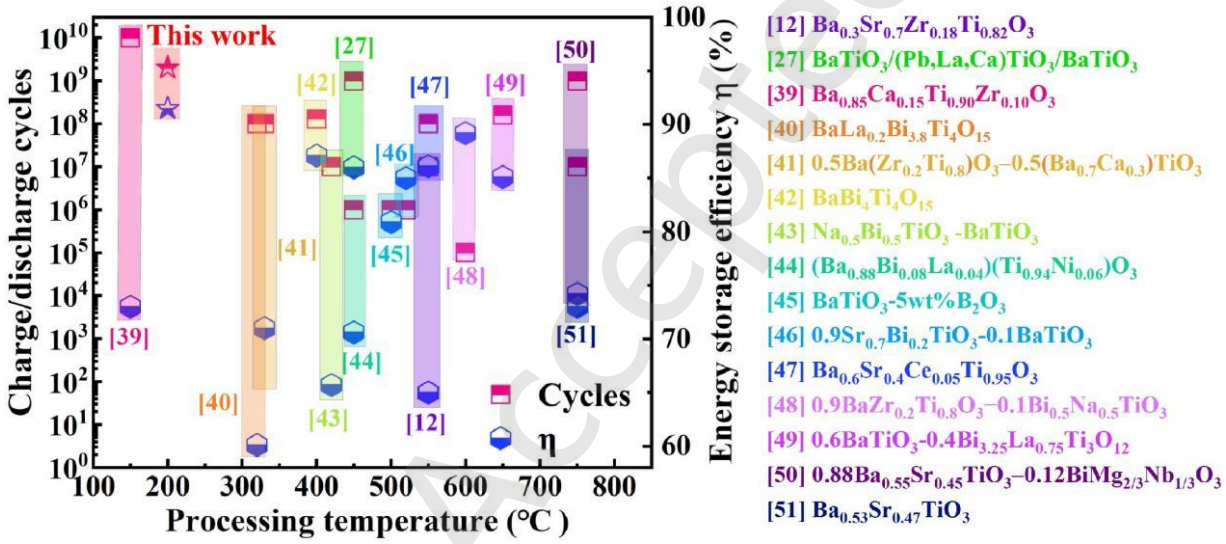

Fig. 8 Systematic comparison of energy storage efficiency (η), charge/discharge cycles and processing temperature compatibility between the BTO/BZT/BTO sandwich film in this work and some reported representative BTO- and BZT-based thin films, including doping, multilayer and solid solution systems.

4 Conclusions

This work focused on the long-standing technical bottlenecks of ferroelectric thin film capacitors, including the trade-off between energy storage density and efficiency, and particularly poor integration compatibility. Through an innovatively engineered design of sandwich BTO/BZT/BTO heterostructure with a low thermal budget, the polarization behavior was modulated via an unique microstructure featured by spatially gradient-distributed nano-columnar crystallites in an amorphous-dominated matrix. Consequently, the BTO/BZT/BTO sandwich film with superior energy storage properties was

fabricated via radio-frequency magnetron sputtering at a low processing temperature of 200 ℃. This constructed sandwich film effectively delayed saturation of polarization, postponed electric breakdown process, and reduced dielectric nonlinearity, thereby achieving a remarkable enhancement in overall energy storage properties, including a substantial recoverable energy density W_{rec} of 100.6 J/cm^3 with a high efficiency η of 90.9%, an enhanced breakdown electric field E_b of 6.1 MV/cm, a broad operating frequency- and temperature-window, notably a robust cycling reliability (2×10^9 cycle). Critically, this work successfully integrates semiconductor processing compatibility (low-thermal-budget of ≤300 ℃ in this study) with excellent energy storage properties, showing a great application potential for high-power pulsed systems and high-energy-density integrated electronic devices.

Acknowledgements

The authors acknowledge the funding support of Natural Science Foundation of Shandong Province (No. ZR2025MS931), National Natural Science Foundation of China (NSFC) (Nos. 92463306, 52402149). H. Zhu is also grateful for the support of Key Innovation Project of the Science-Education-Industry Integration Pilot Engineering of Qilu University of Technology (Shandong Academy of Sciences) (No. 2025ZDZX08).

Author contributions

Methodology, data curation, investigation, formal analysis, writing-original draft: Huali Liu, Li Li.

Data curation, investigation, visualization: Xing Zhao, Ying Liu.

Formal analysis, investigation: Haijian Wang, Zhongshuo Xia, Chenxi Li, Zixu Yang.

Funding acquisition, investigation, methodology, supervision: Hanfei Zhu, Jianting Li.

Resources: Hanfei Zhu, Jianting Li, Hui Liu, Gang Liu.

Conceptualization, data curation, funding acquisition, investigation, methodology, supervision, writing-review & editing: Hanfei Zhu.

All authors contributed the general discussions and analyses of the experimental data.

Availability of data and materials

The data that support the findings of this study are available from the corresponding author upon reasonable request.

Competing interests

The authors have no competing interests to declare that are relevant to the content of this article.

Electronic Supplementary Material (ESM)

Electronic Supplementary Material: Supplementary material is available in the online version of this article.

References

[1] Kim J, Saremi S, Acharya M, *et al.* Ultrahigh capacitive energy density in ion-bombarded relaxor ferroelectric films. *Science* 2020, **369**: 81–84.

[2] Zhang M, Lan S, Yang B, *et al.* Ultrahigh energy storage in high-entropy ceramic capacitors with polymorphic relaxor phase. *Science* 2024, **384**: 185–189.

[3] Zhang L, Jing R, Zhang S, *et al.* Multiscale microstructure design for high-performance dielectric energy storage materials. *Microstructures* 2026, **6**: 2026003.

[4] Palneedi H, Peddigari M, Hwang G, *et al.* High-performance dielectric ceramic films for energy storage capacitors: progress and outlook, *Adv Funct Mater* 2018, **28**: 1803665.

[5] Long C, Zhou W, Song H, *et al.* Simultaneously realizing ultrahigh energy storage density and efficiency in $BaTiO_3$-based dielectric ceramics by creating highly dynamic polar nanoregions and intrinsic conduction. *Acta Mater* 2023, **256**: 119135.

[6] Chen Q, Cheng M, Su P, *et al.* Entropy engineering in ferroelectric/dielectric superlattices for

ultrahigh-efficiency superparaelectrics energy storage capacitors. *Microstructures* 2026, **6**: 2026070.

[7] Pan H, Jiang Y, MacManus-Driscoll J. Interplay of polarization, strength, and loss in dielectric films for capacitive energy storage: current status and future directions. *J Materiomics* 2023, **9**: 516–519.

[8] Su Y, Liu Z, Yang D, *et al.* High energy storage under the regulation of polymer phase structure. *Small* 2025, **21**: 2410354.

[9] Cao W, Lin R, Hou X, *et al.* Interfacial polarization restriction for ultrahigh energy-storage density in lead-free ceramics. *Adv Funct Mater* 2023, **33**: 2301027.

[10] Cheng H, Ouyang J, Zhang Y, *et al.* Demonstration of ultra-high recyclable energy densities in domain-engineered ferroelectric films. *Nat Commun* 2017, **8**: 1999.

[11] Ren Y, Cheng H, Ouyang J, *et al.* Bimodal polymorphic nanodomains in ferroelectric films for giant energy storage. *Energy Storage Mater* 2022, **48**: 306–313.

[12] Chen X, Peng B, Ding M, *et al.* Giant energy storage density in lead-free dielectric thin films deposited on Si wafers with an artificial dead-layer. *Nano Energy* 2020, **78**: 105390.

[13] Sedky S, Witvrouw A, Bender H, *et al.* Experimental determination of the maximum post-process annealing temperature for standard CMOS wafers. *IEEE Trans Electron Devices* 2001, **48**: 377–385.

[14] Calzada M, Bretos I, Jiménez R, *et al.* Low-temperature processing of ferroelectric thin films compatible with silicon integrated circuit technology. *Adv Mater* 2004, **16**: 1620–1624.

[15] Zhu H, Zhao Y, Ouyang J, *et al.* Achieving a record-high capacitive energy density on Si with columnar nanograined ferroelectric films. *ACS Appl Mater Interfaces* 2022, **14**: 7805–7813.

[16] Zhao Y, Ouyang J, Wang K, *et al.* Achieving an ultra-high capacitive energy density in ferroelectric films consisting of superfine columnar nanograins. *Energy Storage Mater* 2021, **39**: 81–88.

[17] Wang K, Zhu H, Ouyang J, *et al.* Significantly improved energy storage stabilities in nanograined ferroelectric film capacitors with a reduced dielectric nonlinearity. *Appl Surf Sci* 2022, **581**: 152400.

[18] Wang K, Zhang Y, Wang S, *et al.* High energy performance ferroelectric (Ba,Sr)(Zr,Ti)O_3 film capacitors integrated on Si at 400 °C. *ACS Appl Mater Interfaces* 2021, **13**: 22717–22727.

[19] Liu C, Ouyang J, Zhao Y, *et al.* Achieving a large field-induced polarization and energy density in $BaTiO_3$ films sputter-deposited on Si at 200 °C via a buffer-layer technique. *J Adv Ceram* 2025, **14**: 9221038.

[20] Wang Y, Zhu H, Luo H, *et al.* Tunable antiferroelectric-like polarization behavior and enhanced energy storage characteristics in symmetric $BaTiO_3$/$BiFeO_3$/$BaTiO_3$ heterostructure, *J Materiomics* 2024, **10**: 1290–1298.

[21] Zhu H, Liu M, Zhang Y, *et al.* Increasing energy storage capabilities of space-charge dominated ferroelectric thin films using interlayer coupling. *Acta Mater* 2017, **122**: 252–258.

[22] Luo H, Niu M, Zhu H, *et al.* Temperature-modulated crystallographic orientation and electrical properties of $BiFeO_3$ thick films sputtered on $LaNiO_3$/Pt/Ti/SiO_2/Si for piezo-MEMS applications, *J Adv Ceram* 2024, **13**: 1943–1954.

[23] Yang C, Chen M, Hong T, *et al.* Preparation of (100)-oriented metallic $LaNiO_3$ thin films on Si substrates by radio frequency magnetron sputtering for the growth of textured Pb($Zr_{0.53}Ti_{0.47}$)O_3. *Appl Phys Lett* 1995, **66**: 2643–2645.

[24] Wakiya N, Azuma T, Shinozaki K, *et al.* Low-temperature epitaxial growth of conductive $LaNiO_3$ thin films by RF magnetron sputtering. *Thin Solid Films* 2002, **410**: 114–120.

[25] Zhu H, Yang Y, Ren W, *et al.* Rhombohedral $BiFeO_3$ thick films integrated on Si with a giant electric polarization and prominent piezoelectricity. *Acta Mater* 2020, **200**: 305–314.

[26] McMillen M, Douglas A, Correia T, *et al.* Increasing recoverable energy storage in electroceramic capacitors using “dead-layer” engineering. *Appl Phys Lett* 2012, **101**: 242909.

[27] Liu J, Wang Y, Zhu H, *et al.* Synergically improved energy storage performance and stability in sol–gel processed $BaTiO_3$/(Pb,La,Ca)TiO_3/$BaTiO_3$ tri-layer films with a crystalline engineered sandwich structure. *J Adv Ceram* 2023, **12**: 2300–2314.

[28] Sengupta S, Ghatak A, Raychaudhuri A. Effect of low temperature structural phase transitions in $BaTiO_3$ on electrical transport through a metal–ferroelectric–metal multilayer of AuCr/$BaTiO_3$/Nb:$SrTiO_3$. *J Phys Condens Mat* 2021, **33**: 465702.

[29] Wang J, Fang H, Nie F, *et al.* Domain switching in $BaTiO_3$ films induced by an ultralow mechanical force. *ACS Appl Mater Interfaces* 2022,**14**: 48917–48925.

[30] Cai H, Yan S, Zhou M, *et al.* Significantly improved energy storage properties and cycling stability in La-doped $PbZrO_3$ antiferroelectric thin films by chemical pressure tailoring. *J Eur Ceram Soc* 2019, **39**: 4761–4769.

[31] Qian J, Ge G, Cai Z, *et al.* Constructing topological vortex domains in polar nano-regions enables high-capacitive energy storage. *Adv Mater* 2026, **38**: e18813.

[32] Xie A, Zuo R, Qiao Z, *et al.* $NaNbO_3$-($Bi_{0.5}Li_{0.5}$)TiO_3 lead-free relaxor ferroelectric capacitors with superior energy-storage performances via multiple synergistic design. *Adv Energy Mater* 2021, **11**: 2101378.

[33] Dai S, Li M, Wu X, *et al.* Combinatorial optimization of perovskite-based ferroelectric ceramics for energy storage applications, *J Adv Ceram* 2024, **13**: 877-910.

[34] Sun Z, Ma C, Liu M, *et al.* Ultrahigh energy storage performance of lead-free oxide multilayer film capacitors via interface engineering, *Adv Mater* 2017, **29**: 1604427.

[35] Li D, Jiang X, Hao H, *et al.* Amorphous/crystalline engineering of $BaTiO_3$-based thin films for energy- storage capacitors. *ACS Sustainable Chem Eng* 2022, **10**: 1731-1740.

[36] Liu Y, Qian J, Guo Y, *et al.* High energy storage density achieved in polymer composites by hierarchical interface engineering design. *Chem Eng J* 2025, **505**: 159343.

[37] Qian J, Han Y, Yang C, *et al.* Energy storage performance of flexible NKBT/NKBT-ST multilayer

film capacitor by interface engineering, *Nano Energy* 2020, **74**: 104862.

[38] Yang M, Guo M, Xu E, *et al.* Polymer nanocomposite dielectrics for capacitive energy storage. *Nat Nanotechnol* 2024, **19**: 588–603.

[39] Reddy S, Prasad V, Bysakh S, *et al.* Superior energy storage performance and fatigue resistance in ferroelectric BCZT thin films grown in an oxygen-rich atmosphere. *J Mater Chem C* 2019, **7**: 7073–7082.

[40] Tang Z, Chen J, Yang B, *et al.* Energy storage performances regulated by layer selection engineering for doping in multi-layered perovskite relaxor ferroelectric films. *Appl Phys Lett* 2019, **114**: 163901.

[41] Silva J, Silva J, Oliveira M, *et al.* High-performance ferroelectric–dielectric multilayered thin films for energy storage capacitors. *Adv Funct Mater* 2019, **29**: 1807196.

[42] Song D, Yang J, Yang B, *et al.* Energy storage in $BaBi_4Ti_4O_{15}$ thin films with high efficiency, *J Appl Phys* 2019, **125**: 134101.

[43] Tang Z, Ge J, Ni H, *et al.* High energy-storage density of lead-free $BiFeO_3$ doped $Na0.5Bi_{0.5}TiO_3$-$BaTiO_3$ thin film capacitor with good temperature stability. *J Alloys Compd* 2018, **757**: 169–176.

[44] Zhang J, Huang R, Tao C, *et al.* Ultra-high energy storage density $BaTiO_3$ amorphous thin film via multi-ion synergistic optimization. *Ceram Int* 2023, **49**: 34969–34975.

[45] Wang H, Huang R, Hao H, *et al.* Reinforced via the insulative boric oxide in the $BaTiO_3$ amorphous thin film with high energy storage capability and stability. *Ceram Int* 2023, **49**: 9260–9267.

[46] Zhou J, Zhu H, Wang J, *et al.* Optimized energy storage performance of SBT-based lead-free relaxor ferroelectric thin film, *J Mater Sci Mater Electron* 2023, **34**: 1294.

[47] Ge S, Liu S, Feng W, *et al.* Achieving high energy storage performance and thermal stability concurrently in the cost-cutting $Al_2O_3/Ba_{0.6}Sr_{0.4}Ti_{0.95}Ce_{0.05}O_3/ZrO_2$ composite films for energy storage applications. *Ceram Int* 2023, **49**: 9155–9164.

[48] Chen Y, Huang R, Tao C, *et al.* Simultaneously achieved high energy density and efficiency in $(1-x)BaZr_{0.2}Ti_{0.8}O_3-xBi_{0.5}Na_{0.5}TiO_3$ thin films with good stability via amorphous-structure engineering. *J Mater Sci Mater Electron* 2023, **34**: 1256.

[49] Yang B, Guo M, Song D, *et al.* Energy storage properties in $BaTiO_3$-$Bi_{3.25}La_{0.75}Ti_3O_{12}$ thin films. *Appl Phys Lett* 2018, **113**: 183902.

[50] Liu G, Li Y, Shi M, *et al.* An investigation of the dielectric energy storage performance of $Bi(Mg_{2/3}Nb_{1/3})O_3$-modifed $BaTiO_3$ Pb-free bulk ceramics with improved temperature/frequency stability. *Ceram Int* 2019, **45**: 19189–19196.

[51] Zhu X, Guo M, Sun B, *et al.* Significantly enhanced energy storage density of epitaxial $Ba_{0.53}Sr_{0.47}TiO_3$ thin films by optimizing bottom electrode material. *Ceram Int* 2020, **46**: 13900–13906.